Realistic nonlocal refrigeration engine based on Coulomb-coupled systems

Anamika Barman,[*] Surojit Halder, Shailendra K. Varshney, Gourab Dutta, and Aniket Singha[*,†]
Department of Electronics and Electrical Communication Engineering, Indian Institute of Technology Kharagpur, Kharagpur 721302, India

(Received 16 May 2020; revised 15 August 2020; accepted 22 December 2020; published 25 January 2021)

We investigate, in detail, a triple quantum dot system that exploits Coulomb coupling to achieve nonlocal refrigeration. The system under investigation is a derivative of the nonlocal thermodynamic engine, originally proposed by Sánchez and Büttiker [Phys. Rev. B **83**, 085428 (2011)], that employs quadruple quantum dots to attain efficient nonlocal heat harvesting. Investigating the cooling performance and operating regime using the quantum master equation approach, we point out some crucial aspects of the refrigeration engine. In particular, we demonstrate that the maximum cooling power for the setup is limited to about 70% of the optimal design. Proceeding further, we point out that to achieve a target reservoir temperature lower than the average temperature of the current path, the applied voltage must be greater than a given threshold voltage V_{TH} that increases with the decrease in the target reservoir temperature. In addition, we demonstrate that the maximum cooling power, as well as the coefficient of performance, deteriorates as one approaches a lower target reservoir temperature. The triple quantum dot system, investigated in this paper, combines fabrication simplicity along with descent cooling power and may pave the way towards the practical realization of efficient nonlocal cryogenic refrigeration systems.

DOI: 10.1103/PhysRevE.103.012131

I. INTRODUCTION

With scaling technology rapidly invading the nanodomain, the tremendous rise in dissipated heat density and hence operating temperature has drawn significant attention to electrical refrigeration in nanoscale dimensions [1–29]. In addition, sophisticated experiments on exploratory technologies, such as quantum computation, spin and optics based computation, etc., occasionally call for electrical refrigeration at cryogenic temperatures in the nanometer range length scale. However, the refrigeration performance in such nanoscale systems is often affected drastically by the large lattice heat flux, particularly when both the region of refrigeration and heat dissipation lie along the path of current flow and are separated by a few nanometers in space. Despite lots of effort to reduce lattice thermal conductance [30–41], the performance of refrigeration nanosystems is still affected by rapid reverse heat flux. This effect poses a threat to the refrigeration performance as device channels are gradually invading the nanodomain. An attempt to improve the refrigeration performance by engineering lattice thermal conductance generally deteriorates the electronic conductivity and hence the cooling power. As an alternative, one of the major research foci, concerning a nanoscale refrigeration engine, is to facilitate independent manipulation of the electron transport path and lattice heat conduction path by introducing spatial separation between the current path and the target reservoir [2,3,6–8,42–44]. This phenomenon of refrigerating a remote target reservoir, which is spatially separated from the current track, is known as nonlocal refrigeration [2,3,6–8,42–44]. Thus, nonlocal refrigeration systems are three-terminal systems in which input power is delivered between two terminals to extract heat from a remote target reservoir through the third terminal. In this case, optimizing the lattice heat transport path, in an attempt to improve refrigeration performance, can be accomplished without modifying the current conduction path. These kinds of systems thus enable independent optimization of the lattice thermal conductance and the current conductivity [2,3,6–8,42–44]. In addition, due to the nonlocality of the electronic transport path, the refrigerated region is significantly shielded from reverse heat flux owing to the Joule dissipation.

Sánchez and Büttiker proposed and demonstrated the optimal nonlocal thermodynamic engine based on Coulomb-coupled systems in the literature [1]. Subsequently, Zhang *et al.* analyzed the effect of suboptimal conditions on the refrigeration performance of the nonlocal thermodynamic engine in detail [2]. Soon, various proposals for realistic construction and implementation of suitable conditions for optimal operation of the nonlocal refrigeration engine were put forth. Such proposals include exploitation of reservoirs with a gapped density of states, superconducting reservoirs, and quantum dot filters to achieve efficient refrigeration [3–5]. Subsequent analysis of heat engine driven nonlocal refrigeration and the effect of cotunneling on the refrigeration performance was carried out in Refs. [6–8]. Recently, experimental demonstration of a nonlocal heat and refrigeration engine was also carried out in Refs. [45–47].

As stated above, the system configuration for the optimal operation of the nonlocal heat and refrigeration engine was elaborated in the literature by Sánchez and Büttiker [1]. In addition, Sánchez and Büttiker also conceived the idea and considered the practical possibility of achieving efficient

[*]These authors contributed equally to this work.
[†]aniket@ece.iitkgp.ac.in

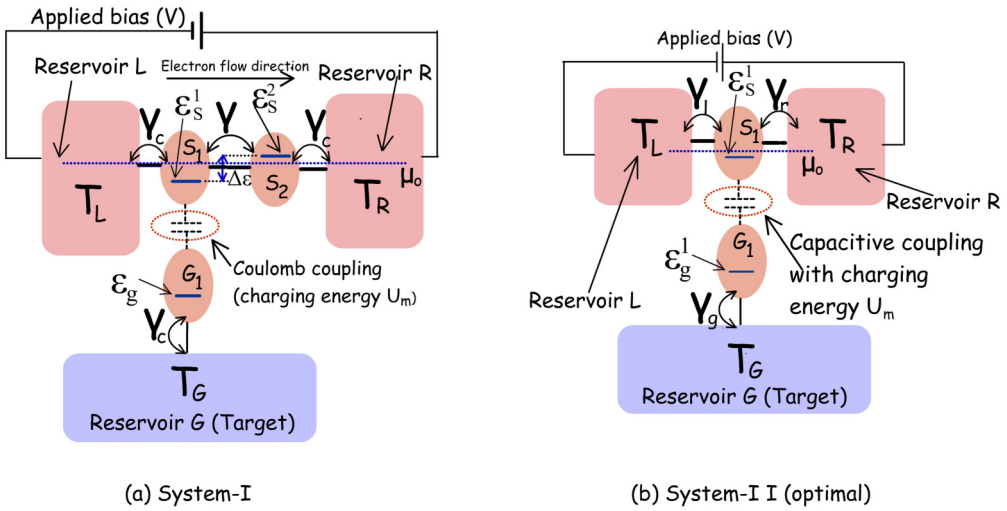

FIG. 1. (a) Schematic of the triple quantum dot refrigeration engine under consideration in this paper. The system consists of triple dots S_1, S_2, and G_1, which are electrically coupled to the macroscopic electron reservoirs L, R, and G, respectively. S_1 is tunnel coupled to S_2 and capacitively coupled to G_1. The tunnel-coupled quantum dots S_1 and S_2 share a staircase ground state configuration with $\varepsilon_s^2 = \varepsilon_s^1 + \Delta\varepsilon$. We will designate this setup as system I. (b) Schematic of the recently proposed optimal refrigerator using Coulomb-coupled systems [1]. This refrigeration engine consists of two Coulomb-coupled quantum dots, S_1 and G_1. S_1 is coupled to reservoirs L and R with coupling energy γ_l and γ_r, respectively. Dot G_1 is electrically connected to the remote reservoir G via coupling energy γ_g and capacitively coupled to S_1 with Coulomb coupling energy U_m. We will call this system II.

nonlocal heat harvesting, and hence refrigeration, by employing a quadruple quantum dot setup, where two additional quantum dots serve as energy filters. However, a compact and detailed investigation on the performance of such proposed strategies has not been conducted to date. In this paper, we investigate, in detail, a Coulomb-coupled system based setup [depicted in Fig. 1(a) as system I] that employs triple quantum dots to achieve efficient nonlocal refrigeration. Although a derivative of the quadruple quantum dot refrigeration engine originally conceived and proposed by Sánchez and Büttiker [1], the triple quantum dot system ensures fabrication simplicity by employing only a single quantum dot filter instead of dual filters. The refrigeration engine is theoretically analyzed using the quantum master equation approach for such systems in the sequential tunneling limit [48]. It is demonstrated that the maximum cooling power (heat extracted per unit time) for the investigated triple quantum dot refrigeration engine (system I) is limited to about 70% of that for the optimal design [depicted in Fig. 1(b) as system II] [1]. We note that the triple quantum dot setup (system I) integrates fabrication simplicity along with decent cooling power, making such a design suitable for practical implementation and applications. At the end, the sequential transport phenomena leading to performance deterioration of the setup are investigated.

This paper is organized as follows. In Sec. II, we briefly describe the configuration of system I along with the transport formulation employed to analyze the performance of the refrigeration engine. In Sec. III, we investigate the performance and region of operation of the refrigeration engine for two different cases: (i) $T_G = T_{L(R)}$ and (ii) $T_G < T_{L(R)}$. This section also presents a performance comparison of the demonstrated refrigeration engine (system I) with the optimal setup proposed in the literature [1] in addition to an investigation of the sequential processes leading to performance deterioration of system I. Finally, we conclude this paper briefly in Sec. IV.

II. DESIGN AND TRANSPORT FORMULATION

The nonlocal refrigeration engine, which will be investigated in this paper, is schematically illustrated in Fig. 1(a) as system I. Here, three quantum dots, S_1, S_2, and G_1, are electrically coupled with electronic reservoirs L, R, and G, respectively, with G being the target reservoir to be refrigerated. S_1 and S_2 are tunnel coupled to each other, while G_1 is capacitively coupled to S_1 by suitable fabrication techniques. The capacitive coupling between S_1 and G_1 permits energy exchange while obstructing any particle swap between the dots. The electrically coupled dots S_1 and S_2 may be suitably fabricated or gated to retain a staircase ground state configuration with $\varepsilon_s^2 = \varepsilon_s^1 + \Delta\varepsilon$. We will demonstrate via numerical calculations and theoretical arguments that in the system detailed above, refrigeration of the target reservoir G can be achieved by forcing a net electronic flow from L to R; that is, refrigeration can be achieved at a terminal nonlocal to the current path. The excess energy $\Delta\varepsilon = \varepsilon_s^2 - \varepsilon_s^1$, required for the electrons to tunnel from S_1 to S_2, is extracted from reservoir G via Coulomb coupling. Coming to the fabrication feasibility of such a system, due to the recent progress in nanofabrication techniques, coupled systems employing multiple (more than two) quantum dots, with and without Coulomb coupling, have already been experimentally realized [49–54]. In addition, it has been experimentally demonstrated that spatially and electrically isolated quantum dots may be bridged to obtain strong Coulomb coupling, in addition to excellent thermal insulation [55–58]. Also, the bridge may be constructed between two specific dots to radically increase their mutual Coulomb

coupling, without affecting the electrostatic potential of the other quantum dots [55–58]. Thus, the fluctuation in electron number n_{S_1} (n_{G_1}) of dot S_1 (G_1) alters the electrostatic energy of dot G_1 (S_1). The total increase in electrostatic energy U of the configuration, consisting of three dots, due to fluctuation in electron number can be given by [48,59]

$$U(n_{S_1}, n_{G_1}, n_{S_2}) = \sum_x U_x^{\text{self}} \left(n_x^{\text{tot}} - n_x^{\text{eq}}\right)^2 + \sum_{(x_1,x_2)}^{x_1 \neq x_2} U_{x_1,x_2}^m \left(n_{x_1}^{\text{tot}} - n_{x_1}^{\text{eq}}\right)\left(n_{x_2}^{\text{tot}} - n_{x_2}^{\text{eq}}\right),$$

where n_x^{tot} is the total electron number at finite temperature and n_x^{eq} is the total electron number under equilibrium conditions at 0 K in dot x (satisfying the condition that the system equilibrates at the minimum possible value of electrostatic energy at 0 K). $U_x^{\text{self}} = \frac{q^2}{C_x^{\text{self}}}$ is the electrostatic energy due to self-capacitance C_x^{self} (with the adjacent terminals) of quantum dot x, and U_{x_1,x_2}^m is the mutual electrostatic energy between two spatially separated quantum dots, x_1 and x_2. $n_x = n_x^{\text{tot}} - n_x^{\text{eq}}$ is the number of excess electrons in the ground state of dot x due to thermal fluctuations (kicks) from the reservoirs at finite temperature. To investigate the performance of the refrigeration engine, we consider a minimal physics based model to simplify our calculations. We assume that the electrostatic energy due to self-capacitance is much greater than V or kT/q, i.e., $U_x^{\text{self}} \gg (kT, qV)$, where $T = \frac{T_{L(R)}+T_G}{2}$, such that electron occupancy probability or transfer rate across the Coulomb blocked energy level due to self-capacitance is negligibly small. Hence, the ground state of a particular dot can be occupied by, at most, one electron, and the behavior of the entire system can be analyzed via $2^3 = 8$ different multielectron states. These states may be denoted $|n_{S_1}, n_{G_1}, n_{S_2}\rangle = |n_{S_1}\rangle \otimes |n_{G_1}\rangle \otimes |n_{S_2}\rangle$, where $n_{S_1}, n_{G_1}, n_{S_2} \in (0, 1)$ indicate the number of electrons in the ground state of S_1, G_1, and S_2, respectively. We consider that the Coulomb coupling between S_1-S_2 and S_2-G_1 is negligible compared to the relevant energy scales of the system; that is, electrostatic coupling between S_1 and S_2 and S_2 and G_1 is negligible with respect to U_{S_1,G_1}^m, kT, and qV. Thus, for all practical purposes related to electron transport $U_{S_1,S_2}^m \approx 0$, and $U_{G_1,S_2}^m \approx 0$. Due to capacitive coupling, the electronic transports through S_1 and G_1 are interdependent, and hence, the pair of dots S_1 and G_1 is treated as a subsystem (ς_1) of the entire system, with S_2 being the complementary subsystem labeled ς_2 [48]. The probability of the subsystem ς_1 to be in a particular state is denoted by $P_{i,j}^{\varsigma_1}$, where i and j are the number of electrons in the ground state of dots S_1 and G_1, respectively. On the other hand, $P_k^{\varsigma_2}$ denotes the steady-state occupancy probability of dot S_2 (subsystem ς_2). Under the condition that $\Delta\varepsilon$ is much higher than the ground state broadening due to reservoir coupling, the optimal interdot tunneling between S_1 and S_2 occurs when $\Delta\varepsilon = U_{S_1,G_1}^m$, such that $\varepsilon_s^2 = (\varepsilon_s^1 + U_{S_1,G_1}^m)$ [48]. Hence, for the optimal performance investigation of the demonstrated system I, we assume $\Delta\varepsilon = U_{S_1,G_1}^m$. In what follows, we refer to U_{S_1,G_1}^m as simply U_m to make the notations compact. Under the assumption that interdot electron transport between S_1 and S_2 can occur only when the ground state of G_1 is occupied [59], the equations dictating the steady state subsystem probabilities can be obtained as follows [48]:

$$\begin{aligned}
&-P_{0,0}^{\varsigma_1}\left\{f_L(\varepsilon_s^1) + f_G(\varepsilon_g^1)\right\} + P_{0,1}^{\varsigma_1}\left\{1 - f_G(\varepsilon_g^1)\right\} + P_{1,0}^{\varsigma_1}\left\{1 - f_L(\varepsilon_s^1)\right\} = 0,\\
&-P_{1,0}^{\varsigma_1}\left\{1 - f_L(\varepsilon_s^1) + f_G(\varepsilon_g^1 + U_m)\right\} + P_{1,1}^{\varsigma_1}\left\{1 - f_G(\varepsilon_g^1 + U_m)\right\} + P_{0,0}^{\varsigma_1} f_L(\varepsilon_s^1) = 0,\\
&-P_{0,1}^{\varsigma_1}\left\{1 - f_G(\varepsilon_g^1) + f_L(\varepsilon_s^1 + U_m) + \frac{\gamma}{\gamma_c}P_1^{\varsigma_2}\right\} + P_{0,0}^{\varsigma_1} f_G(\varepsilon_g^1) + P_{1,1}^{\varsigma_1}\left\{1 - f_L(\varepsilon_s^1 + U_m) + \frac{\gamma}{\gamma_c}P_0^{\varsigma_2}\right\} = 0,\\
&-P_{1,1}^{\varsigma_1}\left\{\left[1 - f_G(\varepsilon_g^1 + U_m)\right] + \left[1 - f_L(\varepsilon_s^1 + U_m)\right] + \frac{\gamma}{\gamma_C}P_0^{\varsigma_2}\right\} + P_{1,0}^{\varsigma_1} f_G(\varepsilon_g^1 + U_m) + P_{0,1}^{\varsigma_1}\left\{f_L(\varepsilon_s^1 + U_m) + \frac{\gamma}{\gamma_c}P_1^{\varsigma_2}\right\} = 0, \qquad (1)
\end{aligned}$$

$$\begin{aligned}
&-P_0^{\varsigma_2}\left\{f_R(\varepsilon_s^2) + \frac{\gamma}{\gamma_c}P_{1,1}^{\varsigma_1}\right\} + P_1^{\varsigma_2}\left\{1 - f_R(\varepsilon_s^2) + \frac{\gamma}{\gamma_c}P_{0,1}^{\varsigma_1}\right\} = 0,\\
&-P_1^{\varsigma_2}\left\{1 - f_R(\varepsilon_s^2) + \frac{\gamma}{\gamma_c}P_{0,1}^{\varsigma_1}\right\} + P_0^{\varsigma_2}\left\{f_R(\varepsilon_s^2) + \frac{\gamma}{\gamma_c}P_{1,1}^{\varsigma_1}\right\} = 0, \qquad (2)
\end{aligned}$$

where γ and γ_c are the associated magnitudes of the interdot and system-to-reservoir coupling, respectively [48,59,60], and $f_\zeta(\epsilon)$ is the statistical occupancy probability of the reservoir ζ at energy ϵ. For the purposes of our present calculations, we assume quasiequilibrium electron statistics at the reservoir, and hence, the function $f_\zeta(\epsilon)$ is the Fermi-Dirac function for the corresponding quasi-Fermi level at reservoir ζ:

$$f_\zeta(\epsilon) = \left\{1 + \exp\left(\frac{\epsilon - \mu_\zeta}{kT_\zeta}\right)\right\}^{-1}, \qquad (3)$$

where T_ζ and μ_ζ are the temperature and quasi-Fermi energy of the reservoir ζ, respectively. Both (1) and (2) form dependent sets of equations, which can be broken by employing the probability conservation rules $\sum_{i,j=0,1} P_{i,j}^{\varsigma_1} = 1$ and $\sum_{k=0,1} P_k^{\varsigma_2} = 1$. The sets of equations (1) and (2) form a nonlinear set of equations and should be solved using any iterative numerical method. For the purposes of our present calculation, the Newton-Raphson scheme was used to calculate the system steady-state probabilities $P_{i,j}^{\varsigma_1}$ and $P_k^{\varsigma_2}$. On calculation of steady-state probabilities the charge current

between the system and the reservoirs $I_{L(R)}$ and the heat current I_{Qe} (extracted from reservoir G) can be calculated as

$$I_L = \frac{q^2}{h}\gamma_c\{P_{0,0}^{\varsigma_1} f_L(\varepsilon_s^1) + P_{0,1}^{\varsigma_1} f_L(\varepsilon_s^1 + U_m)\} - \frac{q^2}{h}\gamma_c\{P_{1,0}^{\varsigma_1}\{1 - f_L(\varepsilon_s^1)\} - P_{1,1}^{\varsigma_s^1}\{1 - f_L(\varepsilon_s^1 + U_m)\}\}, \tag{4}$$

$$I_R = -\frac{q^2}{h}\gamma_c\{P_0^{\varsigma_2} f_R(\varepsilon_s^1) - P_1^{\varsigma_2}\{1 - f_R(\varepsilon_s^1)\}\}, \tag{5}$$

$$I_{Qe} = U_m \frac{q\gamma_c}{h}\{P_{1,0}^{\varsigma_1} f_G(\varepsilon_g + U_m) - P_{1,1}^{\varsigma_1}\{1 - f_G(\varepsilon_g + U_m)\}\}, \tag{6}$$

where q is the electronic change and h designates Plank's constant. In Eq. (6), we have also neglected the reverse heat flux due to lattice thermal conductivity, assuming ideal thermal insulation of reservoir G with its surroundings. It should be noted that the heat extracted per unit time from reservoir G, given in Eq. (6), is not directly dependent on the ground state ε_g of G_1 due to the fact that the net current into (or out of) reservoir G is zero. As described, to achieve refrigeration in reservoir G, a net electronic flow has to be injected from L to R. To achieve such electron flow, a voltage bias can be applied between L and R with the negative and positive terminals of the bias connected to terminals L and R, respectively.

We now briefly discuss the electronic transport processes resulting in the refrigeration of reservoir G. Let us consider that the system is in the initial state $|0, 0, 0\rangle$, which we also call the vacuum state. A sequence of electronic transport that extracts a heat packet U_m from reservoir G is as follows: $|0, 0, 0\rangle \rightarrow |1, 0, 0\rangle \rightarrow |1, 1, 0\rangle \rightarrow |0, 1, 1\rangle \rightarrow |0, 1, 0\rangle \rightarrow |0, 0, 0\rangle$. In this sequence, the system starts with the vacuum state. Next, an electron is injected into S_1 with an energy ε_s^1 followed by an electron injection in G_1 with an energy $\varepsilon_g + U_m$. Next, the electron in S_1 gets transferred to S_2 via interdot tunneling and subsequently flows out of terminal R. The system returns to the initial vacuum state when the electron in G_1 tunnels out to G with an energy ε_g. Note that in this cycle, the electron is injected into G_1 from G with energy $\varepsilon_g + U_m$ and extracted back into G with energy ε_g. Thus, reservoir G loses a packet of heat energy U_m. Such a transport process and other equivalent sequential processes lead to refrigeration of reservoir G. Thus, to achieve refrigeration, a net electronic flow needs to be injected from reservoir L to R, which calls for application of bias voltage with polarity shown in Fig. 1(a). Application of an external bias configuration, as demonstrated in Fig. 1(a), shifts the reservoir quasi-Fermi energy as $\mu_L = \mu_0 + qV/2$, $\mu_R = \mu_0 - qV/2$, and $\mu_G = \mu_0$, where μ_L, μ_R, and μ_G denote the quasi-Fermi energy of reservoirs L, R, and G, respectively, while μ_0 denotes the Fermi energy of the entire setup in the equilibrium condition.

When analyzing the refrigeration performance, two parameters of prime importance constitute the cooling power or the heat extracted per unit time I_{Qe} [defined in Eq. (6)] and the rate of heat extracted per unit input power, which is also known as the coefficient of performance (COP) of the refrigerator. The total input power P is dependent on the bias voltage as well as the injected current and can be defined as

$$P = I_{L(R)} \times V, \tag{7}$$

where V is the applied bias voltage across reservoirs L and R. As stated above, the efficiency of a refrigerator is normally characterized by its COP:

$$C_P = \frac{I_{Qe}}{P}, \tag{8}$$

where the heat extracted per unit time from G can be calculated using Eq. (6).

III. RESULTS

In this section, we describe the performance and operation regime of the demonstrated refrigeration engine (system I). Without loss of generality, we assume that $\gamma_c = 10^{-6}$ eV and $\gamma = 10^{-5}$ eV. Such values of γ and γ_c imply the weak coupling limit and thus suppress any coherent oscillations and restrict the electronic transport in the sequential tunneling regime where the effects of cotunneling and higher-order tunneling can be neglected [61,62]. In addition, we also compare the performance of our design (system I) with the optimal nonlocal refrigeration engine (system II) discussed in the literature [1] and elaborate the transport processes affecting the refrigeration performance of system I. The optimal refrigeration engine, depicted in Fig. 1(b) as system II, consists of two quantum dots, S_1 and G_1 [1]. S_1 is electrically coupled to reservoirs L and R with coupling strengths γ_l and γ_r, respectively, while G_1 is electrically coupled to reservoir G with coupling strength γ_g. To compare the refrigeration performance of system I with system II, the reservoir-to-dot interfaces of system II are assumed to have the optimal filtering properties [1] with $\gamma_l = \gamma_c\theta(\varepsilon_s^1 + \delta\varepsilon - \epsilon)$, $\gamma_r = \gamma_c\theta(\epsilon - \varepsilon_s^1 - \delta\varepsilon)$, and $\gamma_g = \gamma_c$, where ϵ indicates the independent energy variable, θ is the Heaviside step function, and $\delta\varepsilon < U_m$.

Analysis of performance and regime of operation. Figures 2 and 3 demonstrate the operation regime of the refrigeration engine for low bias ($V = 0.2\frac{kT}{q}$) and high bias ($V = 10\frac{kT}{q}$) conditions, respectively, for Coulomb coupling energy $U_m = 3\frac{kT}{q}$ and $T_{L(R)} = T_G = T = 10$ K. In particular, Figs. 2(a) and 2(b) demonstrate the cooling power I_{Qe} and the COP, respectively, over a range of ground state positions for ε_s^1 and ε_g. It can be noted from Fig. 2(a) that the regime of refrigeration corresponds to ε_s^1 lying within a few kT around μ_0. Such a trend occurs since the rate of electron transport through the system, under low bias conditions, peaks when the ground states of the quantum dots lie within a few kT of the equilibrium Fermi energy μ_0. We also note that the refrigeration power is finite and large when ε_g lies within a few kT of the equilibrium Fermi energy μ_0. Such behavior occurs due to the fact that for extraction of heat energy from G, an electron must be able to tunnel into and out of G_1 with energy $\varepsilon_g + U_m$ and ε_g, respectively. Hence, both functions $f_G(\varepsilon_g + U_m)$ and $1 - f_G(\varepsilon_g)$ must have finite values, which is possible only if ε_g lies within a few kT of the equilibrium Fermi energy μ_0. In fact, the product $f_G(\varepsilon_g + U_m)\{1 - f_G(\varepsilon_g)\}$ is maximized when $\varepsilon_g - \mu_0 = -\frac{U_m}{2}$. Since $U_m \approx \frac{3kT}{q}$ in this case, we note the maximum cooling power occurs around $\varepsilon_g - \mu_0 = -\frac{3kT}{2q}$.

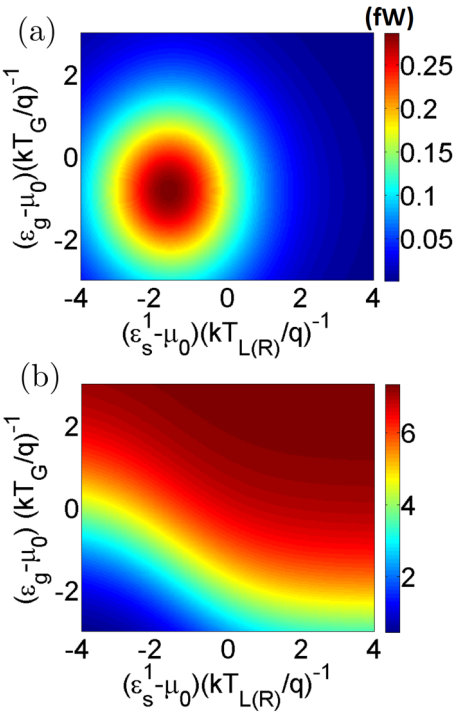

FIG. 2. Regime of refrigeration of the demonstrated design (system I) for the low bias condition ($V = 0.2\frac{kT}{q}$) with $T_L = T_R = T_G = T = 10$ K. Color plots showing the variation of (a) cooling power I_{Qe} and (b) the COP with the position of the ground states ε_g and ε_s^1 for $V = 0.2\frac{kT}{q}$ (≈0.17 meV) and $U_m = 3\frac{kT}{q}$ (≈2.5 meV).

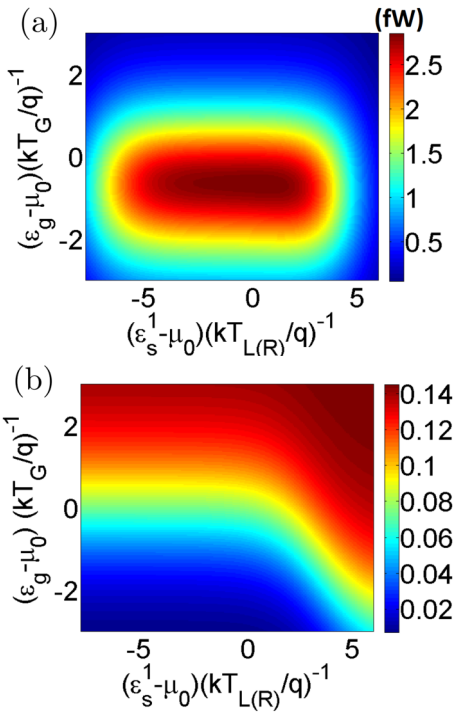

FIG. 3. Regime of refrigeration of the demonstrated design (system I) for the high bias condition ($V = 10\frac{kT}{q}$) with $T_L = T_R = T_G = T = 10$ K. Color plots showing the variation of (a) cooling power I_{Qe} and (b) the COP with the position of the ground states ε_g and ε_s^1 for $V = 10\frac{kT}{q}$ (≈8.5 meV) and $U_m = 3\frac{kT}{q}$ (≈2.5 meV).

Figure 2(b) demonstrates the variation in the COP for the low bias condition. We note a monotonic increase in the COP with ε_g and ε_s^1. Figures 3(a) and 3(b) demonstrate the cooling power and the COP for the high bias condition with $V = 10\frac{kT}{q}$. We note that with an increase in bias voltage V, the refrigeration engine now operates over a wide range of ε_s^1, mainly due to an increase in the energy range over which net electron transport can occur between reservoirs L and R. The operation regime, in terms of ε_g, however, remains almost identical to the low bias case. The COP shows a similar trend with the low bias case; that is, the COP increases with ε_g and ε_s^1. By comparing Figs. 2 and 3 we note a drastic increase (about 10 times) in the maximum cooling power. This is due to the fact that an increase in bias voltage causes more electrons to flow between L and R, which increases the rate of heat absorption from G. The COP, on the other hand, decreases drastically with an applied bias voltage. This can be explained by the fact that an increase in the bias voltage causes a higher power dissipation per unit electron flow qV or per unit heat packet U_m absorption from G, which results in a decrease in the COP. To get more physical insights into the phenomena, the variation in current flow through the setup against variation in ε_s^1 and ε_g is plotted in Appendix A for low and high bias conditions. It should be noted that an equivalent trend of increase in refrigeration power and decrease in the overall COP with an increase in bias voltage can also be noted for lower-dimensional and bulk Peltier refrigerators [27,28].

The variation in maximum cooling power of the refrigeration engine with variation in the Coulomb coupling energy U_m and applied bias voltage is demonstrated in Fig. 4. In particular, Figs. 4(a) and 4(b) demonstrate the maximum cooling power I_{Qe}^M for a range of values of the applied bias voltage V and the Coulomb coupling energy U_m for (i) $T_G = T_{L(R)}$ and (ii) $T_G < T_{L(R)}$, respectively. To achieve the maximum cooling power the ground states of the dots are adjusted to the optimal position with respect to the equilibrium Fermi energy for each value of applied bias V and Coulomb coupling energy U_m. In Fig. 4(a), the maximum cooling power is low for low values of U_m. Despite a high current for lower values of U_m [48], the total cooling power is low due to a low value of the average heat extracted per unit electron flow. As U_m increases, the net rate of electron flow decreases for the same value of bias voltage V [48]. However, the average heat extracted per unit electron flow increases with U_m. These two competing processes result in an initial increase in cooling power with an increase in U_m. With a further increase in U_m beyond a certain limit, the cooling power finally decreases due to a decrease in the total current flowing through the system. From the perspective of the dot G_1, it can be stated that the net cooling power decreases with an increase in U_m beyond a certain limit due to a lower probability of electrons tunneling into gate G_1 with energy $\varepsilon_g + U_m$ when the ground state of S_1 is already occupied. Comparing Figs. 4(a) and 4(b), we indicate certain noteworthy points in the refrigeration performance for the case $T_G < T_{L(R)}$. First of all, the cooling power is nonzero only when the voltage exceeds a certain minimum value, which we call the threshold voltage V_{TH}. The origin of such a threshold bias for refrigeration lies in the appearance of an open-circuit

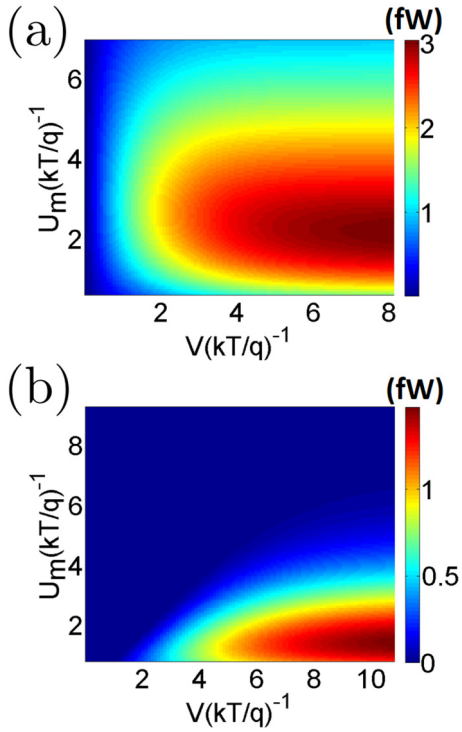

FIG. 4. Variation in maximum cooling power I_{Qe}^{M} with applied bias V and Coulomb coupling energy U_m for (a) $T_{L(R)} = T_G = 10$ K and (b) $T_{L(R)} = 10$ K and $T_G = 5$ K. To find out the maximum cooling power for a given value of V and U_m, the ground states of the dots are tuned to their optimal position. $T = \frac{T_{L(R)}+T_G}{2}$ is the average temperature between the hot and cold reservoirs. In (a), the lower limit or starting value of U_m has been chosen to be 0.5 meV to ensure the validity of the quantum master equations illustrated in Eqs. (1) and (2) [48,59].

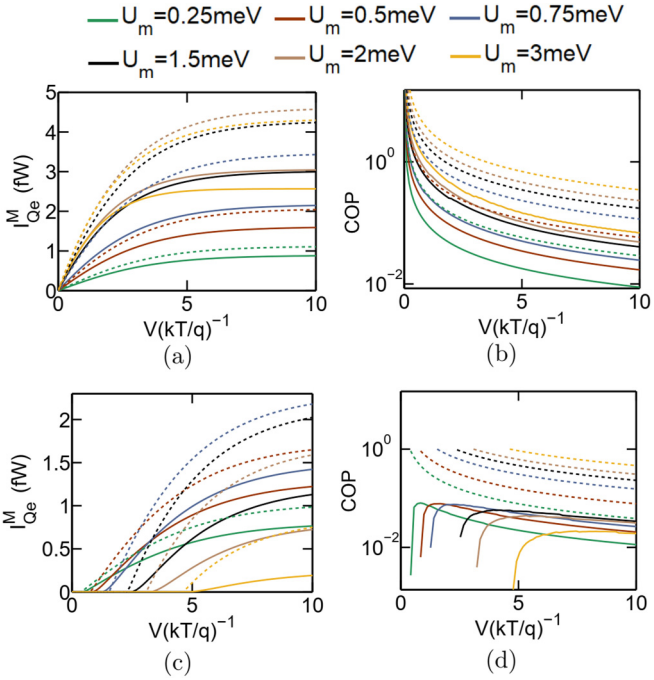

FIG. 5. Comparison of the performance of system I (solid lines) with the optimal setup, that is, system II (dashed lines), for different values of Coulomb coupling energy U_m. (a) Cooling power and (b) the COP (log scale) as a function of bias voltage V at $T_{L(R)} = T_G = 10$ K. (c) Cooling power and (d) the COP (log scale) as a function of bias voltage V at $T_{L(R)} = 10$ K and $T_G = 5$ K.

voltage (due to nonlocal thermoelectric action [59]) with opposite polarity for $T_G < T_{L(R)}$ which tends to drive electrons from R towards L while dumping heat packets into reservoir G [59]. Second, the voltage beyond which nonzero cooling power is achieved increases with the increase in Coulomb coupling energy U_m. This again is due to the increase in the opposite open-circuit voltage in such a setup with an increase in U_m [59]. The applied bias must overcome the open-circuit voltage to effectively cool the reservoir G. Third, the maximum saturation cooling power becomes much lower compared to the case of $T_G = T_{L(R)}$. An exhaustive discussion and analysis of the case of $T_G < T_{L(R)}$ is presented later.

Performance comparison with optimal nonlocal refrigeration engine. Figure 5 demonstrates the performance comparison between the illustrated design and optimal nonlocal refrigeration engine [2,3,6–8] for two different cases: (i) $T_G = T_{L(R)}$ (top row) and (ii) $T_G < T_{L(R)}$ (bottom row). The maximum cooling power I_{Qe}^{M} and COP (in log scale) as a function of bias voltage V are plotted, respectively, in the left and right columns of Fig. 5 for 5 K $= T_G < T_{L(R)} = 10$ K (top row) and $T_G = T_{L(R)} = 10$ K (bottom row) for different values of U_m. Figures 5(a) and 5(c) depict the maximum cooling power for system I (solid lines) and system II (dashed lines) for the cases $T_G = T_{L(R)}$ and $T_G < T_{L(R)}$, respectively. For $T_G = T_{L(R)} = 10$ K, the overall maximum cooling powers for system I and system II are 3 and 4.6 fW, respectively. The overall maximum cooling power in both the setups is achieved at $U_m = 2$ meV ($\approx 2.3\frac{kT_G}{q}$). Similarly, for 5 K $= T_G < T_{L(R)} =$ 10 K, the overall maximum cooling powers for system I and system II are 1.45 and 2.1 fW, respectively. In this case, the maximum cooling power for both setups occurs at $U_m =$ 0.75 meV ($\approx 1.75\frac{kT_G}{q}$). Thus, in both cases, the overall maximum cooling power of system I hovers around 65%–70% of that of that for system II. Figures 5(b) and 5(d) depict the COP (log scale) for system I (solid lines) and system II (dashed lines) for the cases $T_G = T_{L(R)}$ and $T_G < T_{L(R)}$, respectively. We note that the COP for system I is much lower than that of system II. This is because in the case of system I a fraction of the total number of electrons flows from L to R without absorbing heat from reservoir G (explained in the next part).

Sequential tunneling mechanism leading to a performance degradation. Now, we discuss the sequential transport mechanisms leading to a performance degradation of system I. Let us consider the sequence of electron transport from L to R that results in absorbing a heat packet U_m from reservoir G. For example, in the sequence $|0,0,0\rangle \rightarrow |1,0,0\rangle \rightarrow |1,1,0\rangle \rightarrow |0,1,1\rangle \rightarrow |0,1,0\rangle \rightarrow |0,0,0\rangle$, the system initially starts with the vacuum state $|0,0,0\rangle$. An electron is injected from reservoir L into S_1 at energy ε_s^1, followed by another electron injected into G_1 from G with an energy $\varepsilon_g + U_m$. This is followed by the electron in S_1 tunneling into S_2, after which the electron present in G_1 tunnels out into reservoir G with an energy ε_g. At the end of the cycle, the system returns to the vacuum state when the electron present

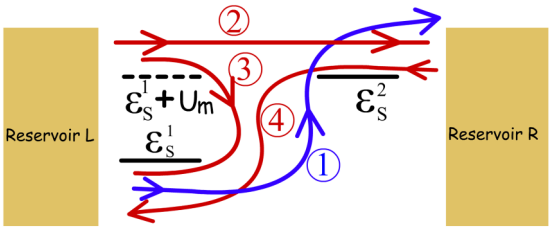

FIG. 6. Schematic diagram demonstrating the different electronic current components from the reservoir L to the system through the energy level ε_s^1 and the Coulomb blockaded level $\varepsilon_s^1 + U_m$ for an applied bias V with $T_G < T_{L(R)}$. Four current components are shown. (1) Electron current flows due to voltage bias from reservoir L to R while absorbing a heat packet U_m (per electron) from G. (2) Electron current, due to applied bias, flows directly from L to R without any heat absorption. (3) and (4) Electron current flows due to the reverse open-circuit voltage for $T_G < T_{L(R)}$. This voltage component appears due to $\Delta T = T_{L(R)} - T_G$ and tends to drive electrons while dumping the heat packet U_m into reservoir G.

in S_2 tunnels out, with energy $\varepsilon_s^2 = \varepsilon_s^1 + U_m$, into R. Thus, in the entire process illustrated above an electron is transmitted from reservoir L to R while absorbing a heat packet U_m from G. These types of transport processes contribute to refrigeration of the target reservoir G and are illustrated as component 1 in Fig. 6. The second electron transport component, depicted in Fig. 6 as component 2, results in direct transmission of electrons between L and R without absorption of heat packets from G. This component flows due to bias voltage. Hence, this component results in wastage of power, thereby causing degradation of the COP. Next, let us consider the following sequence of electron transport: $|0,0,0\rangle \rightarrow |0,1,0\rangle \rightarrow |1,1,0\rangle \rightarrow |1,0,0\rangle \rightarrow |0,0,0\rangle$. In the above sequence, an electron tunnels, with an energy ε_g, into G_1 from reservoir G. This is followed by an electron entering S_1, from reservoir L, with an energy $\varepsilon_s^1 + U_m$. At the next step, the electron present in G_1 tunnels out into reservoir G with energy $\varepsilon_g + U_m$. At the end of the sequence, the electron in S_1 exits into reservoir L with energy ε_s^1. It is evident that in this process, a packet of heat energy U_m is transmitted from reservoir L to G. Thus, this kind of sequence results in heating up of the target reservoir G and is positive and finite only for $T_G < T_{L(R)}$ [59]. This current component, depicted in Fig. 6 as component 3, flows due to the positive temperature difference $\Delta T = T_{L(R)} - T_G$ and affects the refrigeration performance by transmitting heat packets into G. Another current component, which flows for positive $\Delta T = T_{L(R)} - T_G$ while dumping heat packets into G, is shown as component 4 in Fig. 6. From Fig. 6 and the above discussion, it is clear that electron flow components 2 and 3 from L into the Coulomb blockaded level $\varepsilon_s^1 + U_m$ result in degradation of the refrigeration performance.

To further elaborate on the above discussion, we separate out the current flow into the system from reservoir L as

$$I_L = I_1 + I_2,$$

where

$$I_1 = q\gamma_c\{P_{0,0}^{\varsigma_1} f_L(\varepsilon_s^1) - P_{1,0}^{\varsigma_1}[1 - f_L(\varepsilon_s^1)]\},$$
$$I_2 = q\gamma_c\{P_{0,1}^{\varsigma_1} f_L(\varepsilon_s^1 + U_m) - P_{1,1}^{\varsigma^1}[1 - f_L(\varepsilon_s^1 + U_m)]\}. \quad (9)$$

In the above equation, I_1 and I_2 denote the total electron current from reservoir L to the energy level ε_s^1 and the Coulomb blockaded level $\varepsilon_s^1 + U_m$, respectively. Particularly, Figs. 7(a) and 7(b) depict the electron current flow into the system from reservoir L via the energy level ε_s^1 (I_1) and the Coulomb blockaded level $\varepsilon_s^1 + U_m$ (I_2), respectively. Figure 7(c), on the other hand, depicts the overall electronic flow $I_L = I_1 + I_2$ from reservoir L into the system.

We find that the electron current flow I_1 through ε_s^1 into the system from L is positive over a certain regime and negative over the rest. The positive regime corresponds to refrigeration of the target reservoir G. Electronic current flow in this regime, via the energy level ε_s^1, is dominated by component 1 (demonstrated in Fig. 6). The negative regime, on the other hand, has the potential for nonlocal thermoelectric generation where the flux of electrons flows against the voltage bias due to positive $\Delta T = T_{L(R)} - T_G$ [59]. The regime with a negative value of I_1 is dominated by components 3 and 4 through the energy level ε_s^1 and corresponds to no net cooling of the target reservoir G. Interestingly, we also find that the current component I_2 through the Coulomb blockaded energy level $\varepsilon_s^1 + U_m$ is positive, as already shown in Fig. 7(b). This electron current constitutes components 2 and 3 through the Coulomb blocked level $\varepsilon_s + U_m$. As already discussed, these current components result only in deterioration of the net cooling power as well as the COP. Thus, they negatively affect the refrigeration performance. The deterioration in performance of the refrigeration engine due to current components 2 and 3 can be reduced by adding an extra quantum dot filter [1] between L and S_1. However, doing so neutralizes the uniqueness of system I in terms of fabrication simplicity and areal density due to construction of an extra dot and additional gates. In Fig. 7(c), we show the total electronic current flow from L to S_1. It is clear that a very large portion of the total electron flow actually consists of component 2, which results in a lower COP in system I compared to the optimal design (system II). In Fig. 7(d), we demonstrate the heat current flowing out of reservoir G. The positive and negative values of heat current correspond, respectively, to refrigeration and heating of the target reservoir G. Comparing Figs. 7(a) and 7(d), we note that the regimes with positive and negative values of I_1 correspond to refrigeration and generation, respectively, as discussed earlier.

Performance analysis for $T_G < T_{L(R)}$. For a practical electronic refrigeration engine, the target temperature of the reservoir G should generally be less than the environmental temperature or the average temperature of the current path. We have already noted that for positive $\Delta T = T_{L(R)} - T_G$, the applied bias voltage needs to be greater than a certain threshold voltage $V_{\rm TH}$ [59]. Figure 8 demonstrates the refrigeration performance of system I as the temperature of reservoir G is gradually reduced below $T_{L(R)}$. Specifically, Fig. 8(a) depicts the variation in the required threshold voltage $V_{\rm TH}$ to achieve refrigeration. We note from Fig. 8(a) that the threshold voltage $V_{\rm TH}$ is zero for $T_G = T_{L(R)}$ and increases with a decrease in T_G. This is because the open-circuit voltage, which acts opposite to the bias voltage, increases with an increase in $\Delta T = T_{L(R)} - T_G$. Hence, even under ideal conditions of *zero* lattice thermal conductivity, to achieve a lower target temperature T_G

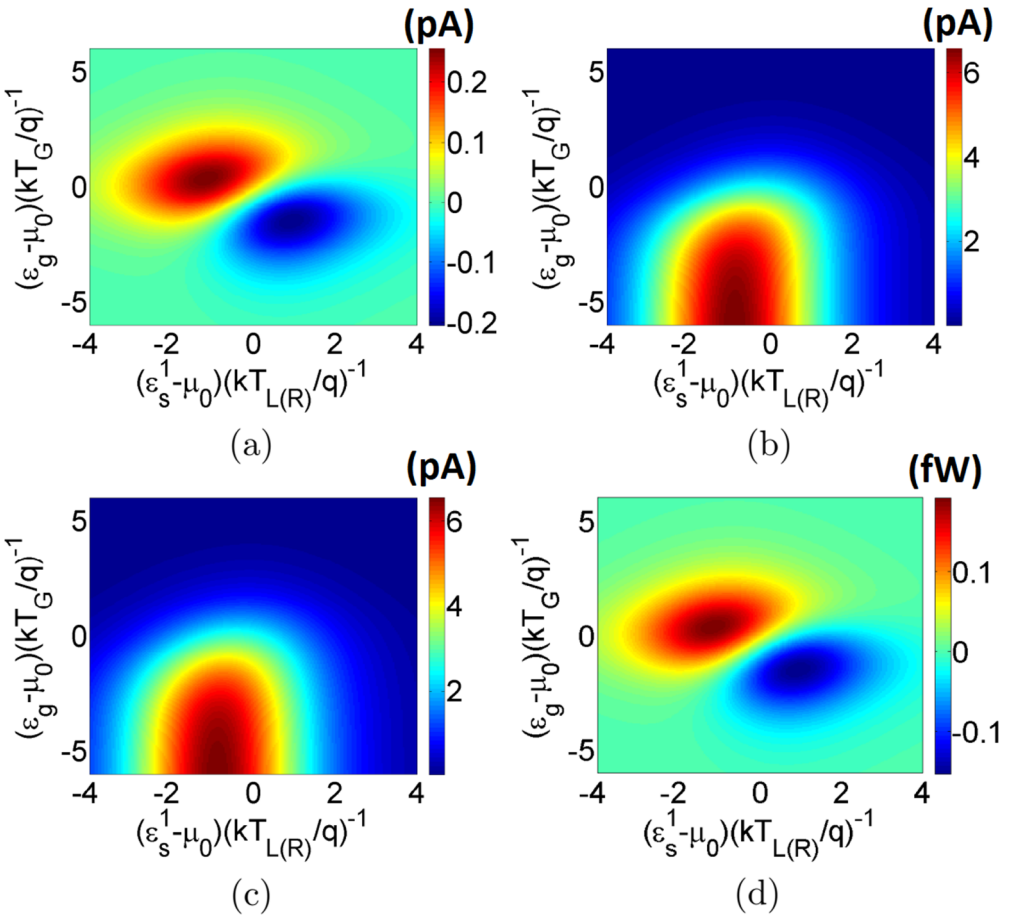

FIG. 7. Plots demonstrating the electronic current flow into the system from reservoir L with variation in the ground states ε_g and ε_s^1. Electronic current flow through (a) the ground state ε_s^1 and (b) the Coulomb blockaded level $\varepsilon_s^1 + U_m$. (c) Total average electron current between the system and reservoir L and (d) heat current flowing out of reservoir G. The regime with positive and negative values of heat current respectively correspond to refrigeration and heating of the target reservoir G. The parameters chosen are $U_m = 0.75$ meV ($\approx 1.16\frac{kT}{q}$) and $V = 1.3$ meV ($\approx 2\frac{kT}{q}$), $T_{L(R)} = 10$ K, and $T_G = 5$ K. $T = \frac{T_{L(R)}+T_G}{2}$ denotes the average temperature between the hot and cold reservoirs.

we need to apply a higher voltage bias V. We also note that the threshold voltage $V_{\rm TH}$ increases with an increase in U_m. This behavior may be attributed to an increase in the reverse open-circuit voltage with an increase in U_m [59]. Figure 8(b) demonstrates the variation in the saturation cooling power (high bias voltage limit) with a decrease in the target temperature T_G for various values of U_m. With a decrease in the target temperature, the saturation cooling power decreases monotonically. In particular, we note that beyond $T_G \leqslant 2$ K, the saturation cooling power for $U_m \geqslant 1.5$ meV is approximately *zero*. This is due to the fact that at very low temperature, the smearing of the Fermi function f_G around μ_0 decreases significantly, making the product $f_G(\varepsilon_g + U_m)\{1 - f_G(\varepsilon_g)\} \approx 0$ for any ε_g at higher values of U_m. We hence conclude that even under ideal conditions, depending on the Coulomb coupling energy U_m, there is a minimum limit beyond which the target temperature T_G cannot be reduced. Figure 8(c) demonstrates the variation of the COP with the target reservoir temperature at the maximum cooling power for $V = \frac{10kT}{q}$. We note that there is a decrease in the COP as one approaches a lower target reservoir temperature, the decrease being more sharper for higher values of U_m. Although not demonstrated in this paper, in the case of $T_G > T_{L(R)}$, the target reservoir G is automatically cooled (due to the nonlocal thermoelectric effect), with T_G gradually approaching $T_{L(R)}$ [59].

IV. CONCLUSION

In this paper, we have investigated a triple quantum dot design for nonlocal refrigeration engine that employs Coulomb coupling to achieve refrigeration. The performance of the demonstrated refrigeration engine was then theoretically investigated employing the quantum master equation formalism. It was demonstrated that the maximum cooling power of the setup hovers around 65%–70% of the optimal design proposed in the literature [2,3,6–8]. Despite a lower cooling power, the key edge of the demonstrated triple quantum dot setup over the optimal design is the integration of fabrication simplicity along with decent refrigeration performance. In our discussion, we have restricted transport phenomena in the weak coupling regime, so that cotunneling processes can be neglected. The refrigeration power in the demonstrated setup can be enhanced by a few orders by tuning electronic transport in the regime of strong coupling, that is, by enhancing the system-to-reservoir and the interdot tunnel coupling. An analysis of the effects of cotunneling and higher order processes on the refrigeration performance

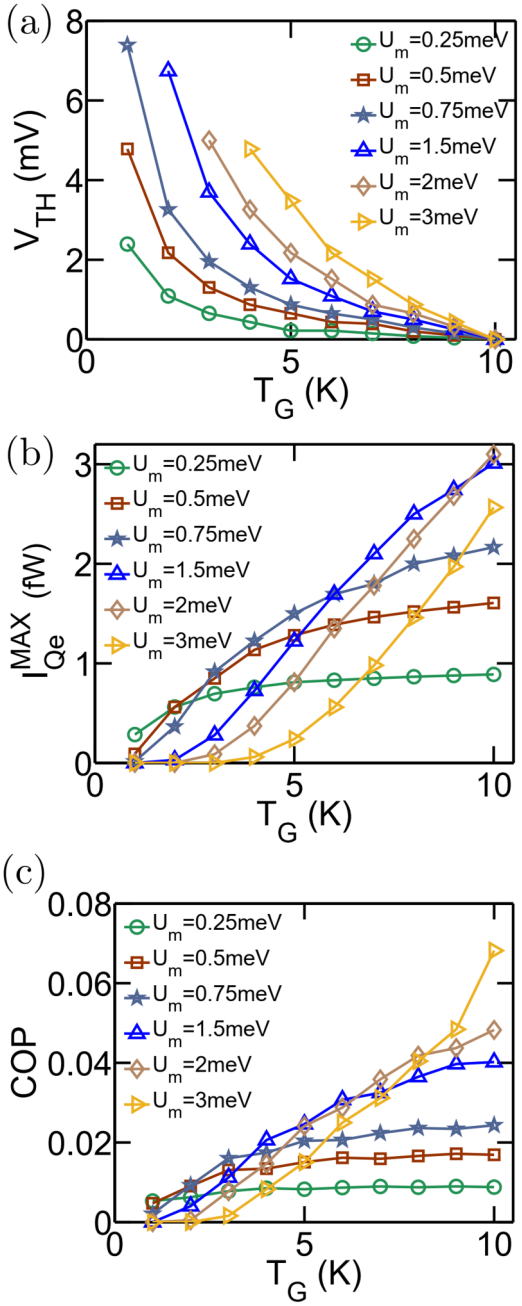

FIG. 8. Performance variation of the demonstrated refrigeration engine (system I) as the target temperature of reservoir G (T_G) gradually decreases below $T_{L(R)} = 10$ K. Variation in (a) threshold voltage $V_{\rm TH}$, (b) overall maximum cooling power $I_{Qe}^{\rm MAX}$, and (c) the COP at the maximum cooling power (for $V = 10\frac{kT_{L(R)}}{q}$) with the decrease in the target temperature T_G of reservoir G. To compute the maximum cooling power for each value of T_G and U_m, the ground states $\varepsilon_{L(R)}$ and ε_G are tuned to their optimal positions.

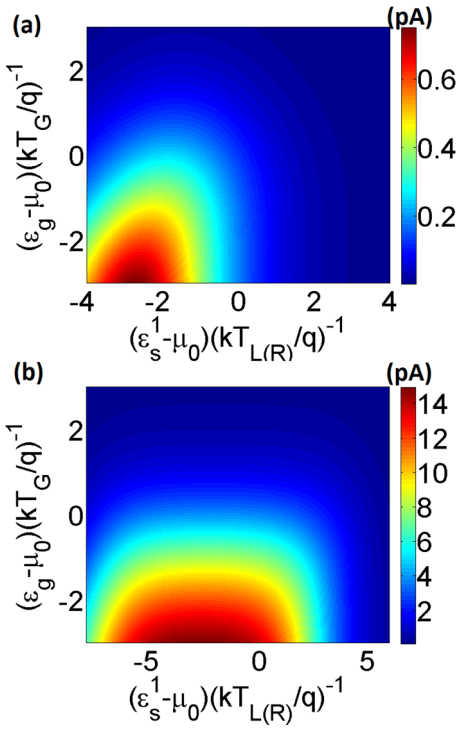

FIG. 9. Variation in current flow through the setup with the position of the ground states ε_g and ε_s^1 for $U_m = 3\frac{kT}{q}$ (≈2.5 meV) under the condition of (a) low bias $V = 0.2\frac{kT}{q}$ (≈0.17 meV) and (b) high bias $V = 10\frac{kT}{q}$ (≈8.5 meV)

of the demonstrated system constitutes an interesting aspect of investigation. Furthermore, an analysis of the impact of electron-phonon scattering [30–41] on the performance of the demonstrated refrigeration engine also constitutes an interesting aspect of future research. The various possible designs for nonlocal refrigeration systems are left for future investigation. Nevertheless, the triple quantum dot design discussed here can be used to realize high performance nonlocal cryogenic refrigeration engines employing Coulomb-coupled systems.

ACKNOWLEDGMENTS

A.S. would like to thank financial support from Sponsored Research and Industrial Consultancy (IIT Kharagpur) via Grant no. IIT/SRIC/EC/MWT/2019-20/162, Ministry of Human Resource Development (MHRD), Government of India via Grant No. STARS/APR2019/PS/566/FS under STARS scheme and Science and Engineering Research Board (SERB), Government of India via Grant No. SRG/2020/000593 under SRG scheme.

APPENDIX A: CURRENT FLOW THROUGH THE SETUP UNDER LOW AND HIGH BIAS CONDITIONS

Figures 9(a) and 9(b) demonstrate the variation in current flow through the system with variation in ε_s^1 and ε_g for the low bias and high bias conditions corresponding to Figs. 2 and 3, respectively. We note from Fig. 9(a) that the current is maximum when $\varepsilon_g - \mu_0$ is a few kT below the Fermi energy and $\varepsilon_s^1 - \mu_0 \approx 3\frac{kT}{q}$, that is when the, ground state ε_g is always occupied and the Coulomb blocked energy level $\varepsilon_s^1 + U_m$ coincides with the Fermi energy. However, we note [from Fig. 2(a)] that the cooling power is low under such conditions because the ground state ε_g is always occupied, and hence, current flows between L and R without absorbing heat from reservoir G. With an increase in ε_g and ε_s^1, the current

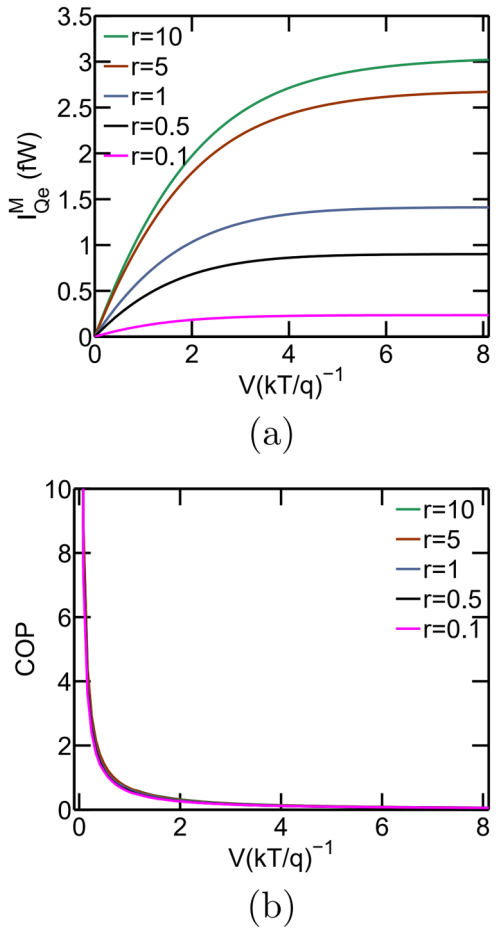

FIG. 10. Performance variation of the refrigeration engine as the ratio $r = \gamma/\gamma_c$ is tuned, keeping the system-to-reservoir coupling constant at $\gamma_c = 10^{-6}$ eV. Plot of (a) maximum cooling power I^M_{Qe} and (b) the COP at the maximum cooling power for various values of r, with variation in the applied voltage for $T_G = T_{L(R)} = 10$ K and $U_m = 2$ meV ($\approx 2.5kT/q$).

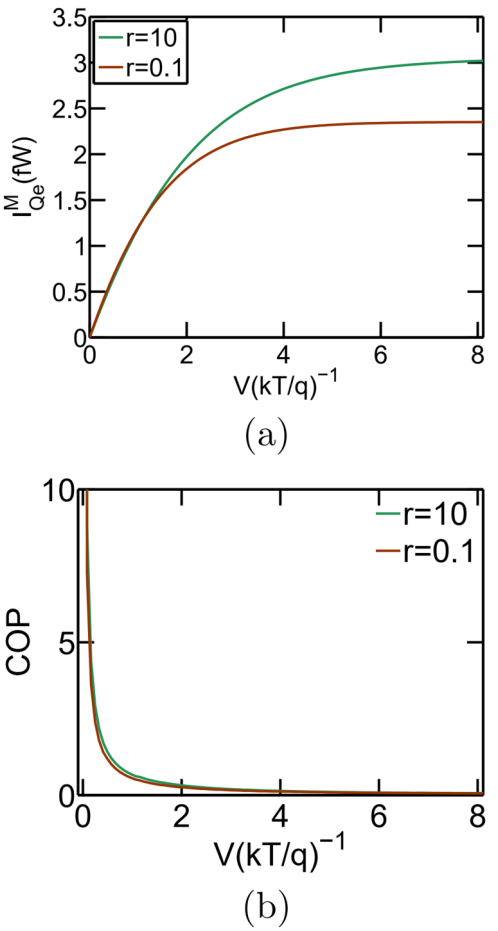

FIG. 11. Performance variation of the refrigeration engine as the values of γ_c and γ are swapped. The two situations illustrated here are (i) $\gamma_c = 10^{-6}$ eV and $\gamma = 10^{-5}$ eV ($r = 10$) and (ii) $\gamma_c = 10^{-5}$ eV and $\gamma = 10^{-6}$ eV ($r = 10$). Plot of (a) maximum cooling power I^M_{Qe} and (b) the COP at the maximum cooling power, with variation in the applied voltage for $T_G = T_{L(R)} = 10$ K and $U_m = 2$ meV ($\approx 2.5kT/q$).

flow through the system decreases, but the refrigeration power increases due to the increase in the stochastic fluctuation in the ground states ε^1_s and ε_g. A further increase in ε_g and ε^1_s causes the cooling power to deteriorate due to the decrease in the total current through the system. A similar inference can be drawn from Fig. 9(b) for the operation regime under the high bias condition (Fig. 3).

APPENDIX B: EFFECT OF THE RATIO $r = \gamma/\gamma_c$ ON THE REFRIGERATION PROPERTIES OF THE TRIPLE QUANTUM DOT SETUP

Here, we discuss the dependence on refrigeration performance of the triple quantum dot setup (system I) with a change in $r = \gamma/\gamma_c$. Until now, the values of the system-to-reservoir and interdot coupling were assumed to be $\gamma_c = 10^{-6}$ eV and $\gamma = 10^{-5}$ eV. Since the overall conductance of the current path is dependent on both γ and γ_c, reducing either of the two affects the refrigeration performance. Figures 10(a) and 10(b) demonstrate the variation in the maximum cooling power I^M_{Qe} and the COP with applied bias V as the ratio $r = \gamma/\gamma_c$ is gradually reduced while keeping γ_c fixed at $\gamma_c = 10^{-6}$ eV. It is expected that for both high and low values of r, the overall conductance of the current path is determined by $\min(\gamma_c, \gamma)$. Thus, for $r \geqslant 10$, the conductance of the current track is mainly controlled by γ_c, and hence, further enhancing the interdot tunnel coupling γ does not have a drastic impact on the refrigeration performance. However, as γ is gradually reduced such that r decreases from $r = 10$, the overall conductance of the current path decreases, resulting in a deterioration in the refrigeration power. Such a trend is noted in Fig. 10(a). From Fig. 10(b), we note that the COP is not strongly dependent on r.

Figure 11 demonstrates the change in refrigeration performance of the system as γ and γ_c are interchanged. In particular, Fig. 11 illustrates the refrigeration performance for two different cases: (i) $\gamma_c = 10^{-6}$ eV and $\gamma = 10^{-5}$ eV, that is, for $r = 10$ (shown in green), and (ii) $\gamma_c = 10^{-5}$ eV and $\gamma = 10^{-6}$ eV, that is, for $r = 0.1$ (shown in brown). We note

that there is a slight deterioration in the saturation cooling power (under the high bias condition) for $r = 0.1$ compared to $r = 10$. The COP, on the other hand, remains almost the same for both cases.

[1] R. Sánchez and M. Büttiker, Phys. Rev. B **83**, 085428 (2011).
[2] Y. Zhang, G. Lin, and J. Chen, Phys. Rev. E **91**, 052118 (2015).
[3] P. A. Erdman, B. Bhandari, R. Fazio, J. P. Pekola, and F. Taddei, Phys. Rev. B **98**, 045433 (2018).
[4] R. Sánchez, Appl. Phys. Lett. **111**, 223103 (2017).
[5] R. Sánchez, P. Samuelsson, and P. P. Potts, Phys. Rev. Research **1**, 033066 (2019).
[6] Y. Zhang and J. Chen, Physica E (Amsterdam, Neth.) **114**, 113635 (2019).
[7] R. Sánchez, H. Thierschmann, and L. W. Molenkamp, New J. Phys. **19**, 113040 (2017).
[8] A.-M. Daré, Phys. Rev. B **100**, 195427 (2019).
[9] G. J. Snyder, E. S. Toberer, R. Khanna, and W. Seifert, Phys. Rev. B **86**, 045202 (2012).
[10] Y. Apertet, H. Ouerdane, A. Michot, C. Goupil, and P. Lecoeur, Europhys. Lett. **103**, 40001 (2013).
[11] A. Shakouri and J. E. Bowers, Appl. Phys. Lett. **71**, 1234 (1997).
[12] A. Shakouri, E. Y. Lee, D. L. Smith, V. Narayanamurti, and J. E. Bowers, Microscale Thermophys. Eng. **2**, 37 (1998).
[13] X. Fan, G. Zeng, E. Croke, G. Robinson, C. LaBounty, A. Shakouri, and J. E. Bowers, in *ITHERM 2000: The Seventh Intersociety Conference on Thermal and Thermomechanical Phenomena in Electronic Systems* (IEEE, Piscataway, NJ, 2000), Vol. 1, p. 307.
[14] X. Fan, G. Zeng, E. Croke, C. LaBounty, D. Vashaee, A. Shakouri, and J. E. Bowers, Electron. Lett. **37**, 126 (2001).
[15] B. De and B. Muralidharan, Sci. Rep. **8**, 5185 (2018).
[16] B. De and B. Muralidharan, J. Phys.: Condens. Matter **32**, 035305 (2019).
[17] B. De and B. Muralidharan, Phys. Rev. B **94**, 165416 (2016).
[18] S. Mukherjee, B. De, and B. Muralidharan, J. Appl. Phys. **128**, 234303 (2020).
[19] R. Kim, C. Jeong, and M. S. Lundstrom, J. Appl. Phys. **107**, 054502 (2010).
[20] J. Zhu and G. Li, Phys. Rev. A **86**, 053828 (2012).
[21] Z.-Z. Li, S.-H. Ouyang, C.-H. Lam, and J. Q. You, Europhys. Lett. **95**, 40003 (2011).
[22] F. Giazotto, T. T. Heikkilä, A. Luukanen, A. M. Savin, and J. P. Pekola, Rev. Mod. Phys. **78**, 217 (2006).
[23] H. L. Edwards, Q. Niu, and A. L. de Lozanne, Appl. Phys. Lett. **63**, 1815 (1993).
[24] K. A. Chao, M. Larsson, and A. G. Malshukov, Appl. Phys. Lett. **87**, 022103 (2005).
[25] R. S. Whitney, Phys. Rev. Lett. **112**, 130601 (2014).
[26] R. S. Whitney, Phys. Rev. B **91**, 115425 (2015).
[27] A. Singha, Phys. Lett. A **382**, 3026 (2018).
[28] A. Singha and B. Muralidharan, J. Appl. Phys. **124**, 144901 (2018).
[29] J. R. Prance, C. G. Smith, J. P. Griffiths, S. J. Chorley, D. Anderson, G. A. C. Jones, I. Farrer, and D. A. Ritchie, Phys. Rev. Lett. **102**, 146602 (2009).
[30] N. Mingo and D. A. Broido, Phys. Rev. Lett. **93**, 246106 (2004).
[31] N. Mingo, Appl. Phys. Lett. **84**, 2652 (2004).
[32] F. Zhou, J. Szczech, M. T. Pettes, A. L. Moore, S. Jin, and L. Shi, Nano Lett. **7**, 1649 (2007).
[33] F. Zhou, A. L. Moore, M. T. Pettes, Y. Lee, J. H. Seol, Q. L. Ye, L. Rabenberg, and L. Shi, J. Phys. D **43**, 025406 (2010).
[34] A. I. Boukai, Y. Bunimovich, J. Tahir-Kheli, J.-K. Yu, W. A. Goddard, and J. R. Heath, Nature (London) **451**, 168 (2008).
[35] A. I. Hochbaum, R. Chen, R. D. Delgado, W. Liang, E. C. Garnett, M. Najarian, A. Majumdar, and P. Yang, Nature (London) **451**, 163 (2008).
[36] A. Balandin, A. Khitun, J. Liu, K. Wang, T. Borca-Tasciuc, and G. Chen, in *Eighteenth International Conference on Thermoelectrics* (IEEE, Baltimore, MD, USA, 1999), pp. 189–192.
[37] G. Chen, Phys. Rev. B **57**, 14958 (1998).
[38] T. Koga, S. B. Cronin, M. S. Dresselhaus, J. L. Liu, and K. L. Wang, Appl. Phys. Lett. **77**, 1490 (2000).
[39] B. L. Davis and M. I. Hussein, Phys. Rev. Lett. **112**, 055505 (2014).
[40] Y. Pan, G. Hong, S. N. Raja, S. Zimmermann, M. K. Tiwari, and D. Poulikakos, Appl. Phys. Lett. **106**, 093102 (2015).
[41] J. P. Feser, J. S. Sadhu, B. P. Azeredo, K. H. Hsu, J. Ma, J. Kim, M. Seong, N. X. Fang, X. Li, P. M. Ferreira, S. Sinha, and D. G. Cahill, J. Appl. Phys. **112**, 114306 (2012).
[42] K. Uchida, H. Adachi, T. Kikkawa, A. Kirihara, M. Ishida, S. Yorozu, S. Maekawa, and E. Saitoh, Proc. IEEE **104**, 1946 (2016).
[43] J. Sinova, S. O. Valenzuela, J. Wunderlich, C. H. Back, and T. Jungwirth, Rev. Mod. Phys. **87**, 1213 (2015).
[44] E. Saitoh, M. Ueda, H. Miyajima, and G. Tatara, Appl. Phys. Lett. **88**, 182509 (2006).
[45] H. Thierschmann, R. Sánchez, B. Sothmann, F. Arnold, C. Heyn, W. Hansen, H. Buhmann, and L. W. Molenkamp, Nat. Nanotechnol. **10**, 854 (2015).
[46] J. V. Koski, A. Kutvonen, I. M. Khaymovich, T. Ala-Nissila, and J. P. Pekola, Phys. Rev. Lett. **115**, 260602 (2015).
[47] B. Roche, P. Roulleau, T. Jullien, Y. Jompol, I. Farrer, D. A. Ritchie, and D. C. Glattli, Nat. Commun. **6**, 6738 (2015).
[48] A. Singha, IOP SciNotes **1**, 025204 (2020).
[49] K. Eng, T. D. Ladd, A. Smith, M. G. Borselli, A. A. Kiselev, B. H. Fong, K. S. Holabird, T. M. Hazard, B. Huang, P. W. Deelman, I. Milosavljevic, A. E. Schmitz, R. S. Ross, M. F. Gyure, and A. T. Hunter, Sci. Adv. **1**, 4 (2015).
[50] H. Flentje, B. Bertrand, P.-A. Mortemousque, V. Thiney, A. Ludwig, A. D. Wieck, C. BÃ¤uerle, and T. Meunier, Appl. Phys. Lett. **110**, 233101 (2017).
[51] F. N. M. Froning, M. K. Rehmann, J. Ridderbos, M. Brauns, F. A. Zwanenburg, A. Li, E. P. A. M. Bakkers, D. M. Zumbühl, and F. R. Braakman, Appl. Phys. Lett. **113**, 073102 (2018).
[52] A. Noiri, K. Kawasaki, T. Otsuka, T. Nakajima, J. Yoneda, S. Amaha, M. R. Delbecq, K. Takeda, G. Allison, A. Ludwig, A. D. Wieck, and S. Tarucha, Semicond. Sci. Technol. **32**, 084004 (2017).
[53] C. Hong, G. Yoo, J. Park, M.-K. Cho, Y. Chung, H.-S. Sim, D. Kim, H. Choi, V. Umansky, and D. Mahalu, Phys. Rev. B **97**, 241115(R) (2018).

[54] T. Takakura, A. Noiri, T. Obata, T. Otsuka, J. Yoneda, K. Yoshida, and S. Tarucha, Appl. Phys. Lett. **104**, 113109 (2014).
[55] A. Hübel, J. Weis, W. Dietsche, and K. v. Klitzing, Appl. Phys. Lett. **91**, 102101 (2007).
[56] I. H. Chan, R. M. Westervelt, K. D. Maranowski, and A. C. Gossard, Appl. Phys. Lett. **80**, 1818 (2002).
[57] L. W. Molenkamp, K. Flensberg, and M. Kemerink, Phys. Rev. Lett. **75**, 4282 (1995).
[58] I. M. Ruzin, V. Chandrasekhar, E. I. Levin, and L. I. Glazman, Phys. Rev. B **45**, 13469 (1992).
[59] A. Singha, J. Appl. Phys. **127**, 234903 (2020).
[60] S. Datta, *Quantum Transport: Atom to Transistor* (Cambridge Press University, Cambridge, 2005).
[61] R. Hussein and S. Kohler, Ann. Phys. (Berlin, Ger.) **527**, 610 (2015).
[62] P. Strasberg, G. Schaller, T. L. Schmidt, and M. Esposito, Phys. Rev. B **97**, 205405 (2018).